

Article

Excellent Performance of Fe₇₈Si₉B₁₃ Metallic Glass for Activating Peroxymonosulfate in Degradation of Naphthol Green B

Xue-Fen Li ^{1,2}, Shun-Xing Liang ¹, Xiao-Wang Xi ², Zhe Jia ¹, Shi-Kun Xie ³, He-Chun Lin ^{4,*}, Jun-Ping Hu ² and Lai-Chang Zhang ^{1,*}

¹ School of Engineering, Edith Cowan University, 270 Joondalup Drive, Joondalup, Perth, WA 6027, Australia; tree0816@163.com (X.-F.L.); shunxinl@our.ecu.edu.au (S.-X.L.); zjia0@our.ecu.edu.au (Z.J.)

² School of Control Technology, Wuxi Institute of Technology, Wuxi 214121, China; xixw@wxit.edu.cn (X.-W.X.); hujp@wxit.edu.cn (J.-P.H.)

³ School of Mechanical and Electrical Engineering, Jinggangshan University, Ji'an 343000, China; xskun@163.com

⁴ Key Laboratory of Polar Materials and Devices, Ministry of Education, East China Normal University, Shanghai 200241, China

* Correspondence: hclin@ee.ecnu.edu.cn (H.-C.L.); lc Zhangimr@gmail.com or l.zhang@ecu.edu.au (L.-C.Z.); Tel.: +86-21-5434-5279 (H.-C.L.); +61-8-6304-2322 (L.-C.Z.)

Received: 19 June 2017; Accepted: 13 July 2017; Published: 17 July 2017

Abstract: The functional application of metallic glasses in the catalytic field has widely attracted research attention due to its unique atomic structure compared to crystalline materials. It has been reported that metallic glasses can effectively activate H₂O₂ and persulfate, yet the activation of peroxymonosulfate by metallic glasses is not studied well. In this work, the metallic glass with atomic composition of Fe₇₈Si₉B₁₃ was applied for investigating the peroxymonosulfate (PMS) activation on degradation of naphthol green B (NGB) dye. The change of surface morphology indicated the important role of oxide films during the dye degradation. The effects and first-order kinetics model of various reaction parameters were evaluated systematically, including PMS concentration, catalyst dosage, irradiation intensity, and dye concentration. The results showed that about 98% of the dye removal rate could be achieved only within 10 min under rational conditions. The reaction kinetics k of 0.1339 min^{−1} without ribbons was sharply improved to 0.3140 min^{−1} by adding 0.5 g/L ribbons, indicating the superior activation ability of Fe₇₈Si₉B₁₃ metallic glass. The recycling experiment revealed that the Fe₇₈Si₉B₁₃ ribbons exhibited the excellent surface stability and catalytic reusability for activating PMS even after reused for 10th run.

Keywords: metallic glass; catalyst; photo-enhanced; peroxymonosulfate activation; oxidative degradation; reusability

1. Introduction

In addition to application as structural materials, the metallic glasses, having their far-from-equilibrium nature and uniquely amorphous atomic packing structure, have been widely employed as functional materials in different fields, such as biodegradable implants [1], aerospace and automobile applications [2], and control devices [3]. Even thin film metallic glasses can be treated as a potential candidate for coatings [4–6]. Very recently, the metallic glasses have been demonstrated as a superior candidate in the field of wastewater treatment attributed to catalytically active and uniquely selective properties, in addition to the easy alteration of chemical compositions [7,8]. For example, ball-milled Co₇₈Si₈B₁₄ glassy powders exhibit excellent performance for completely degrading acid orange II in between 2 to 6 min under different conditions [9]; Mg₇₃Zn_{21.5}Ca_{5.5} glassy powders are

about 1000 times higher than commercial crystalline Fe powders in degrading direct blue 6 dye [10]; $\text{Al}_{91-x}\text{Ni}_9\text{Y}_x$ ($x = 0, 3, 6, 9$ at %) glassy ribbons are able to decolorize direct blue 2B dye solutions in a wide range of pH conditions; with an especially higher decolorization rate in alkaline condition than in neutral [11]. Largely because of the low cost, friendly environmental compatibility, highly anticorrosion ability, and easily reusable operation, Fe-based metallic glasses have been also applied as superior catalysts in wastewater remediation [12–15]. For instance, $\text{Fe}_{73}\text{Si}_7\text{B}_{17}\text{Nb}_3$ glassy powders can completely decompose direct blue 2b with a concentration of 200 mg/L at a very high efficiency with 200 times higher than the conventional Fe powders [16]; $\text{Fe}_{78}\text{Si}_9\text{B}_{13}$ metallic glass/ TiO_2 composite powders can achieve 60% higher decolorization rate than the pure TiO_2 powder in the methylene blue solution degradation [17]. Nanocrystallized Fe-based metallic glasses have also attracted some researchers. Wang et al. [18] reported that nanocrystallized $\text{Fe}_{82.65}\text{Si}_4\text{B}_{12}\text{Cu}_{1.35}$ alloy with the formation of galvanic cells showed a higher efficiency for direct blue 2B degradation than the amorphous counterpart. Simultaneously, Chen et al. [19,20] also demonstrated that an extremely high degree of crystallization of $(\text{Fe}_{73.5}\text{Si}_{13.5}\text{B}_9\text{Nb}_3\text{Cu}_1)_{91.5}\text{Ni}_{8.5}$ metallic glass presented uncommon high reactivity towards dyes due to galvanic cells. For the catalytic sustainability, it is reported that $\text{Fe}_{76}\text{B}_{12}\text{Si}_9\text{Y}_3$ powders with a high removal rate of methyl orange dye only show a slight decay even reused for 13 cycles [21], while $\text{Fe}_{66.3}\text{B}_{16.6}\text{Y}_{17.1}$ glassy foils can completely decolorize orange G dye solution up to 11 cycles [22]. Furthermore, the $\text{Fe}_{78}\text{Si}_9\text{B}_{13}$ ribbons exhibit the excellent reusability for up to 30 cycles in methylene blue decolorization [23]. The advantages of Fe-based metallic glasses employed in the wastewater remediation can be summarized as: (1) ultrafast degradation efficiency of pollutants due to atomic packing structure in amorphous alloy; (2) excellent reusability without apparently catalytic decay after reusing many times due to highly chemical stability [24]; (3) easy to be reused due to soft magnetic property [25]; and (4) negligible secondary sludge produced [26]. Therefore, using Fe-based metallic glasses in wastewater treatment has been an attractive topic.

Over the last few decades, extensive efforts have been made to explore effective wastewater treatment methods, including biological methods (microorganisms, biosorption, etc.) [27,28], physical methods (adsorption on solid phases, ion exchange, etc.) [29–31], and traditional chemical methods (chemical precipitation, electrolysis, etc.) [32]. However, there are still some drawbacks in the traditional wastewater treatment methods, such as the long processing time for biological methods, and high sludge production for physical adsorption and chemical precipitation in addition to not sufficient capacities for dealing with recalcitrant pollutants. Very recently, advanced oxidation processes (AOPs), such as photocatalysis [28,33,34], ozonation [35,36], sulfate-based oxidation [23,26,37], and Fenton/Fenton-like methods [38–41] have been extensively reported as the promising techniques with the rapid degradation efficiency and high mineralization rate on recalcitrant pollutants from industrial wastewater. The AOPs are mostly based on the production of highly reactive species such as hydroxyl radicals ($\bullet\text{OH}$) and/or sulfate radicals ($\text{SO}_4\bullet^-$) to degrade organics compounds into H_2O , CO_2 , and harmless inorganic substances [23,42]. Typically, persulfate (PS), peroxymonosulfate (PMS), and hydrogen peroxide (H_2O_2) are three widely reported source for producing radicals. Sulfate radicals are mainly donated by PS and PMS in the sulfate-based oxidation while hydroxyl radicals are produced by H_2O_2 in the Fenton/Fenton-like processes. Similar to H_2O_2 , PS and PMS can also be activated by transitional metals, especially iron, to produce reactive species. However, traditional iron salts used in those AOPs will produce a large amount of iron sludge, and zero-valent iron (ZVI) powder leads to its high surface oxidation due to the crystalline structure and large specific surface area. Here, as a special ZVI, Fe-based metallic glasses have been reported as an effective activator in the AOPs due to the amorphous atomic packing structure. Recently in our previous work, $\text{Fe}_{78}\text{Si}_9\text{B}_{13}$ glassy ribbons have been investigated as a superior catalyst towards H_2O_2 and PS. Nearly 100% color removal of methyl blue could be reached using a small amount of peroxides (1.0 mmol/L) [23,24]. Yet, the activation of PMS by Fe-based metallic glass have not been investigated and fully understood.

Naphthol green B (NGB), i.e., naphthol green, acid green 1, C.I. 10020 ($C_{30}H_{15}FeN_3Na_3O_{15}S_3$), is an important acid dye. Owing to its bright color, water-fastness and easy coloration, NGB is widely applied as a coloring agent in the leather and fur industries and as a biological stain in modern industry. However, directly discharging NGB dye to the environment will cause serious pollution to aquatic life and mutagenicity to humans [43]. Due to the synthetic and complex aromatic structure, the NGB is difficult to be removed by biodegrading [44]. Furthermore, due to the high pH, high concentration, and high chroma, it is not economically feasible to remove the NGB from industrial wastewater effluents by using conventional methods [43]. Recently, some endeavors using AOPs have been employed to improve the removal efficiency of NGB, such as photocatalytic degradation of NGB by Al-doped ZnO [45], semiconducting Sb_2S_3 [46] and Fe(III) induced by ligand-to-metal charge transfer excitation [47], and photo-Fenton degradation [48]. Nevertheless, those reported photodegradation of NGB cannot achieve satisfying efficiency (up to hours for complete degradation) while the photo-Fenton degradation using Fe^{3+} produces large amounts of iron sludge.

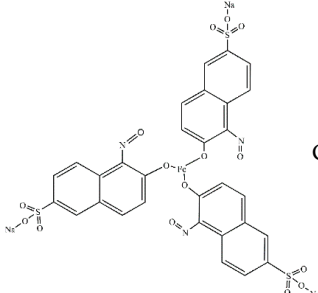
To overcome the disadvantages of aforementioned NGB removal techniques, this work investigated the NGB dye degradation using $Fe_{78}Si_9B_{13}$ /PMS under UV-vis irradiation for promoting the degradation efficiency of NGB. Simultaneously, studying Fe-based metallic glass activation behavior towards peroxymonosulfate including the analysis for those important effects (catalyst dosage, PMS concentration, dye concentration, and irradiation intensity) can provide adequate understanding of heterogeneous sulfate-based oxidation process. In this work, the characterizations of the as-received and reused $Fe_{78}Si_9B_{13}$ ribbons were firstly studied by X-ray diffraction (XRD), ultraviolet visible diffuse reflectance spectrum (UV-vis DRS), scanning electron microscope (SEM), and energy-dispersive X-ray spectroscopy (EDS). The effects and corresponding pseudo-first-order kinetic model of catalyst dosage, PMS concentration, dye concentration, and irradiation intensity on the dye degradation efficiency were systematically examined and discussed in detail. In addition, the stability and reusability of the $Fe_{78}Si_9B_{13}$ ribbons were also studied.

2. Materials and Methods

2.1. Materials and Chemicals

The naphthol green B dye was supplied by Wenzhou Huaqiao Chemical Reagent Co., Ltd., Wenzhou, China. The main characteristics of the dye are summarized in Table 1. Oxone ($KHSO_5 \cdot 0.5KHSO_4 \cdot 0.5K_2SO_4$) was purchased from Sigma-Aldrich. Ethanol (absolute) was obtained from Merck. In this work, the as-received $Fe_{78}Si_9B_{13}$ glassy ribbons, which were cut into 5×20 mm with a thickness of 30–40 μm , were manufactured by the melting spinning method. The master alloy ingot of $Fe_{78}Si_9B_{13}$ was firstly prepared by arc melting under a Ti-gettered argon atmosphere five times to achieve homogenous chemical composition. From the master alloy, the glassy ribbons were fabricated by ejecting melting master alloy on a single copper roller [49–51]. The wheel speed of the copper roller used was about 30 m/s. All the aqueous solutions throughout experiments were prepared using Milli-Q water (18.2 $M\Omega \cdot cm$). All the chemicals used in this work are in analytical grade and no further purification is required.

Table 1. Structure and characteristics of naphthol green B.

Structure	Empirical Formula	Molar Mass (g/mol)	λ_{\max} (nm)
	$C_{30}H_{15}FeN_3Na_3O_{15}S_3$	878.45	714

2.2. Methods

The structure of the as-received and reused $Fe_{78}Si_9B_{13}$ glassy ribbons were identified by XRD. The XRD data were collected on a PANalytical Empyrean diffractometer (Eindhoven, The Netherlands) with monochromated $Co-K\alpha$ radiation ($\lambda = 0.1789$ nm) operated at 40 kV and 40 mA. The UV–vis DRS (Shelton, CT, USA) was employed to examine the surface characterization of as-received and after reused ribbons at the 200–800 nm range using $BaSO_4$ as the reference. The surface morphology of before and reused $Fe_{78}Si_9B_{13}$ ribbons were analyzed by SEM equipped with EDS (JEOL 6000, Tokyo, Japan) with an accelerating voltage of 15 kV. To analyze the catalytic stability and reusability, the $Fe_{78}Si_9B_{13}$ ribbon samples were reused 10 times. After each time, the reused ribbons were washed by Milli-Q water in an ultrasonic cleaner for 3 min, then further carefully cleaned by analytical grade alcohol. All the reused ribbons were preserved in the absolute ethanol for further characterization.

For the dye degradation experiments, 1000 ppm NGB dye solution was firstly prepared and stored in a 500 mL flask for preservation. Then the specific volume of NGB dye solution of 1000 ppm was extracted by a macropipette (SocorexIsba S.A., Ecublens, Switzerland) and diluted to a required dye concentration (10 ppm, 20 ppm, 50 ppm, and 100 ppm). During all the experiments, ribbons with a specific weight (0.03 g, 0.05 g, 0.1 g, and 0.2 g) were immersed into a 100 mL NGB solution under continuous mechanical stirring by Vortex-Genie 2 mixer (Scientific Industries, Inc., New York, NY, USA). The irradiation was provided by a 300 W Xeon simulated solar light lamp (Perfectlight Scientific Pty Ltd., Beijing, China). The pH value of dye solution throughout this work was about 5.8, measured by an Oakton pH/conductivity meter (PC 2700, Cole-Parmer, Vernon Hills, IL, USA). Approximate 3.5 mL NGB dye sample was taken from the beaker at the predetermined time intervals (i.e., 1, 2, 4, 6, 8, 10, 12, 15, 20, and 30 min), then injected into a 3.5 mL quartz cuvette with a pathlength 10 mm, following scanning in turn using a Perkin Elmer Lambda 35 UV–vis spectrometer (Shelton, CT, USA). The wavelength of light absorbance λ_{\max} of NGB was measured at the 408 nm. After the addition of PMS, the peak shifts from 714 to 408 nm due to the acidic nature of PMS. Dye degradation efficiency was calculated by Equation (1):

$$\text{Color Removal (\%)} = [(C_0 - C)/C_0] \times 100\% \quad (1)$$

where C_0 and C are the initial concentration and the concentration at time t (min) of NGB, respectively. The NGB decomposition was fitted by the pseudo-first-order kinetic model as shown in Equation (2), similar to other reports [26,52]:

$$C = C_0 \exp(-k_{\text{obs}}t) \quad (2)$$

where k_{obs} is the calculated reaction rate. The equation of the kinetic model can be rewritten as Equation (3):

$$\ln(C_0/C) = k_{\text{obs}}t \quad (3)$$

3. Results and Discussion

3.1. Characterizations of $\text{Fe}_{78}\text{Si}_9\text{B}_{13}$

The $\text{Fe}_{78}\text{Si}_9\text{B}_{13}$ ribbon samples were reused 10 times for degrading NGB under the same conditions: PMS concentration of 1.0 mmol/L; ribbons dosage of 0.5 g/L; irradiation intensity of $7.7 \mu\text{W}/\text{cm}^2$; and dye concentration of 50 ppm. Then the ribbons were characterized at the specific reused time. Figure 1a shows the XRD patterns of as-received, fifth, and tenth run reused $\text{Fe}_{78}\text{Si}_9\text{B}_{13}$ ribbons. As can be seen, all the XRD patterns present a broad diffraction peak at a range of $2\theta = 40\text{--}60^\circ$, indicating that they are mainly composed of the amorphous phase [53–57]. Clearly, the maximum diffraction peaks at $2\theta = 52.6^\circ$ and 95.7° exhibit a higher diffraction intensity with the increased reused times, which is because crystallized $\alpha\text{-Fe}$ is gradually formed on the surface of the $\text{Fe}_{78}\text{Si}_9\text{B}_{13}$ ribbons during NGB degradation process under the UV–vis irradiation [58,59]. Figure 1b presents the UV–vis DRS patterns of the as-received, fifth and tenth run reused $\text{Fe}_{78}\text{Si}_9\text{B}_{13}$ ribbons. It is known that the tetrahedral or octahedral isolated iron species will cause the bands between 200 and 300 nm, while the octahedral irons in the form of $\text{Fe}^{3+}_x\text{O}_y$ complexes result in the bands between 300 and 450 nm [60,61]. In addition, large iron oxide aggregates may lead to the bands greater than 450 nm [60,61]. In this work, the peaks between 200 and 350 nm of the as-received $\text{Fe}_{78}\text{Si}_9\text{B}_{13}$ ribbons indicate isolated iron species are distributed homogeneously, while no obvious peak after 450 nm means no iron oxide aggregates on the surface. After reused fifth and tenth run, slight peaks after 550 nm are observed in these two $\text{Fe}_{78}\text{Si}_9\text{B}_{13}$ ribbons, indicating that partly iron oxides aggregates (excepting $\alpha\text{-Fe}$) are gradually formed on both ribbons surface. Compared with the as-received $\text{Fe}_{78}\text{Si}_9\text{B}_{13}$ ribbons, the obvious peaks between 200 and 270 nm of the fifth and tenth run reused ribbons indicate that the isolated iron species still distribute homogeneously on the surface, and peaks between 300 and 360 nm are due to octahedral irons presenting as $\text{Fe}^{3+}_x\text{O}_y$ complexes form.

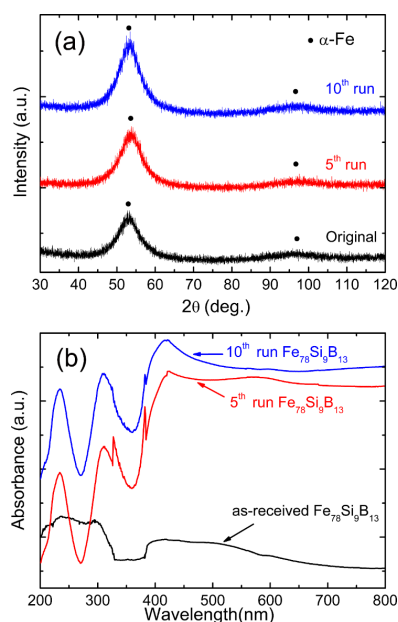


Figure 1. (a) X-ray diffraction (XRD) patterns, (b) ultraviolet visible diffuse reflectance spectrum (UV–vis DRS) of as-received, fifth and tenth run reused $\text{Fe}_{78}\text{Si}_9\text{B}_{13}$ ribbons.

Figure 2a,b shows the SEM and corresponding EDS images of the as-received $\text{Fe}_{78}\text{Si}_9\text{B}_{13}$ ribbons. As seen from Figure 2a, the free surface of the as-received ribbons is practically smooth without any apparent defects. Figure 2b shows the corresponding EDS analysis of as-received ribbons. Apparently, the peaks in the EDS are mainly formed by the element of Fe and Si, and Fe occupies the dominant composition, which is similar to the nominal composition of $\text{Fe}_{78}\text{Si}_9\text{B}_{13}$ ribbons (domination

of Fe). After reused fifth run, the ribbon surface in Figure 2c presents a clear boundary and different layers can be distinguished. The bright area seems like the films which is not adherent to the ribbon surface. According to Figure 2d, it is obvious that after reused fifth run, the ribbon surface has a high concentration of O compared with Figure 2b. Based on the previous research [23,24], it can be confirmed that the region next to the boundary connecting the bright area is covered by the oxide films (iron oxides and silicon dioxide). With the reused time increasing to tenth run, comparing Figure 2e with Figure 2c, the previously distinct boundary disappears. Instead, there are many small pits that can be observed on the ribbon surface (as the enlarged surface in the Figure 2e). Although, the oxide films in the Figure 2e cannot be distinguished easily from its EDS result (Figure 2f), the relatively high concentration of O still demonstrates that the tenth run reused surface is covered by oxide films, but the structure of the film has changed. According to the transformation of surface morphology from as-received ribbons to tenth run reused ribbons, the mechanism of surface change can be concluded as: (1) the as-received ribbon surface is very smooth without any obvious defects; (2) with the reused time increasing, the oxide films due to a series of reactions between Fe and Si, and O_2 are gradually formed on the reused ribbons surface. These oxide films easily fall off from the ribbons surface during the degradation process when being stirred by the mixer; (3) with the loose films exuviating, fresh Fe is exposed to air. Then the Fe continuously goes through a series of reactions to form new compact films; (4) the corrosion of Fe becomes severer with further reactions leading to the formation of pits although the new compact film has strong ability to protect the buried Fe. From Figure 2d,f, compared with the as-received ribbons, the intensity of O increases obviously leading to the total intensity of peaks of Fe and Si on the fifth or tenth run reused ribbons surface is sharply reduced. The possible reasons are: (1) the isolated Fe at the as-received ribbons is gradually corroded during degradation process, leading to the formation of dissociative iron species (Fe^{2+} and Fe^{3+}) and therefore the detected Fe atom on the surface decreases; (2) the application of UV-vis irradiation assists in transferring electron on the $4S^2$ orbital of ribbons due to the extra energy input [24]; (3) PMS has the ability to directly react with isolated Fe. Those corrosion behaviors occur on the ribbons surface concurrently, resulting in an effective and sufficient supplement of iron source to activate PMS.

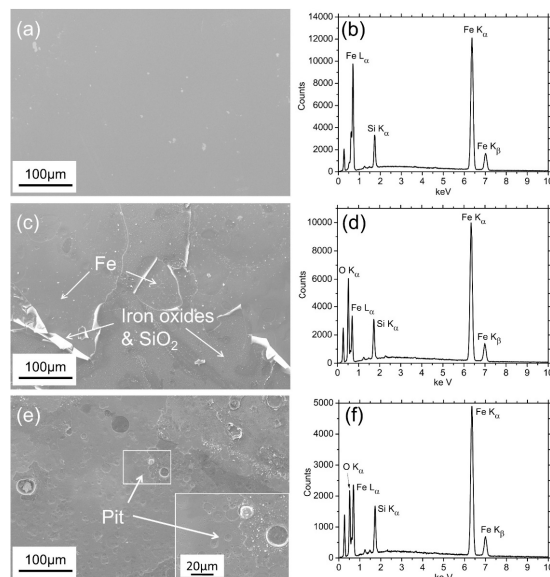


Figure 2. Scanning electron microscope (SEM) micrograph of (a) as-received, (c) fifth run reused and (e) tenth run reused $Fe_{78}Si_9B_{13}$ ribbons; corresponding energy-dispersive spectroscopy (EDS) results of (b) as-received, (d) fifth run reused and (f) tenth run reused $Fe_{78}Si_9B_{13}$ ribbons.

3.2. UV-Vis Spectra

Figure 3 shows the UV-vis spectra of NGB degradation at 0.5 g/L $\text{Fe}_{78}\text{Si}_9\text{B}_{13}$ ribbons within different time intervals (PMS: 1.0 mmol/L, irradiation intensity: $7.7 \mu\text{W}/\text{cm}^2$, dye concentration: 50 ppm). Apparently, with the addition of PMS, a large blue-shift of maximum absorbance peak occurs immediately, from 714 to 408 nm. From the Figure 3, it can be seen that the maximum peak at $\lambda = 408 \text{ nm}$ decreases very fast and become invisible after 10 min reaction time, indicating a progressive removal of the chromophore ($-\text{NO}$) in NGB molecules and a completion after 10 min [47]. In addition, no obvious peak is formed after 10 min and all the previous peaks disappear in both ultraviolet and visible light regions, suggesting that benzene ring opening and cleavage of the central carbon happen at the same time. The result in the UV-vis spectra reveals that the reaction between $\text{Fe}_{78}\text{Si}_9\text{B}_{13}$ ribbons and PMS under UV-vis irradiation can effectively eliminate NGB dye within a very short time, converting dye molecules to harmless inorganic substances.

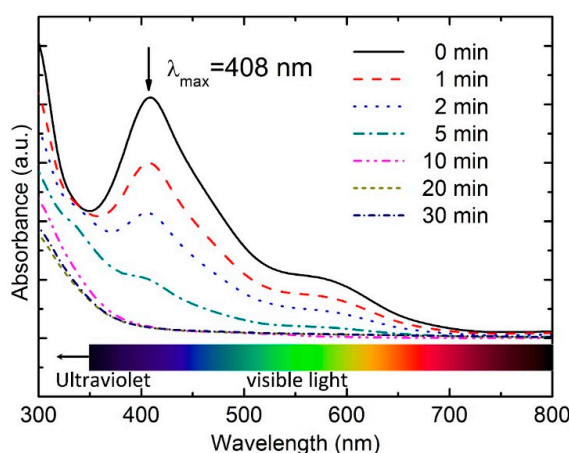


Figure 3. UV-vis spectra of naphthol green B (NGB) dye degradation at different time intervals (peroxymonosulfate (PMS) concentration: 1.0 mmol/L, ribbons dosage: 0.5 g/L, irradiation intensity: $7.7 \mu\text{W}/\text{cm}^2$, dye concentration: 50 ppm).

According to the result in the Figure 3, the removal efficiency of NGB in this work is compared with the other results, which can be seen from the Table 2. It is clear that NGB dye removal using $\text{Fe}_{78}\text{Si}_9\text{B}_{13}$ /PMS under UV-vis irradiation in this work has a faster efficiency which achieves full decolorization within 10 min with a reaction rate $k_{\text{obs}} = 3.14 \times 10^{-1} \text{ min}^{-1}$, while the other results receive a very low efficiency. The required time of fully dye removal is double and more than sextuple for the reported photo-Fenton process [48] and photocatalysis [45,46], respectively, than this work, although all of these methods are based on AOPs. Obviously, the faster NGB degradation by $\text{Fe}_{78}\text{Si}_9\text{B}_{13}$ /PMS system is attributed to aggressively attack by large quantities of reactive species. The comparable result further indicates that $\text{Fe}_{78}\text{Si}_9\text{B}_{13}$ metallic glass is a superior catalyst for activating PMS under UV-vis irradiation.

Table 2. Comparable result of naphthol green B (NGB) removal efficiency by various methods.

Method	Material	Dosage (g/L)	Light Source	Complete Removal Time (min)	k_{obs} (min^{-1})	Reference
Photocatalysis	10% Al-doped ZnO particles	1.0	Solar light	360	5.95×10^{-3}	[45]
Photocatalysis	Semiconducting Sb_2S_3	2.0	Visible light	60	5.37×10^{-2}	[46]
Photo-Fenton process	FeCl_3	0.11	Visible light	>20	1.01×10^{-1}	[48]
Photo-enhanced sulfate-based oxidation	$\text{Fe}_{78}\text{Si}_9\text{B}_{13}$ ribbons	0.5	UV-vis light	10	3.14×10^{-1}	This work

3.3. Single Parameter Effect on Dye Degradation

The degradation process is strongly influenced by the following main operating parameters: PMS concentration; catalyst dosage; irradiation intensity; and dye concentration. In order to study the effect of these parameters systematically, it was investigated by altering the specific parameter while other parameters were constant. All the investigations were compared with the condition (PMS concentration: 1.0 mmol/L; $\text{Fe}_{78}\text{Si}_9\text{B}_{13}$ ribbons dosage: 0.5 g/L; UV-vis irradiation intensity: $7.7 \mu\text{W}/\text{cm}^2$; dye concentration: 50 ppm).

3.3.1. Effect of PMS Concentration

Among the specific reaction parameters of the dye degradation process, the initial concentration of PMS is a key parameter. Figure 4 shows the compared results of PMS concentrations vary from 0 to 2.0 mmol/L. It is found from Figure 4a that only less than 10% of color removal rate could be reached within 30 min when solely using $\text{Fe}_{78}\text{Si}_9\text{B}_{13}$ ribbons at the dosage of 0.5 g/L. It is postulated that the color removal is the consequence of the adsorption property of the ribbons [12], in addition to poor NGB self-photosensitization under UV-vis irradiation [62]. The color removal rate increases remarkably with adding PMS from 0 to 0.25 mmol/L. However, with the low concentration of PMS (0.25 mmol/L), the removal rate of NGB only achieves less than 80% within 15 min and no further increase occurs along the reaction time, while the degradation rate achieves about 94% within 8 min at the 2.0 mmol/L PMS. The first-order kinetic model is shown in Figure 4b and the corresponding data are summarized in Table 3. It can be found that the reaction kinetics (k) value of 1.0 mmol/L PMS is 0.3140 min^{-1} , which is twice as high as the value of PMS (0.25 mmol/L), while the k value is just slightly improved to 0.3509 min^{-1} by increasing the PMS concentration to 2.0 mmol/L, indicating that 1.0 mmol/L PMS is the threshold for effectively degrading NGB dye. Further increase of PMS concentration results in slight effect and both of two PMS concentration (1.0 and 2.0 mmol/L) can achieve almost complete degradation within 10 min. It is known that PMS can act as donor for those reactive species ($\text{SO}_4^{\bullet-}$ and $\bullet\text{OH}$). With increasing PMS concentration, more PMS molecules can be activated to produce $\text{SO}_4^{\bullet-}$ and/or $\bullet\text{OH}$ to degrade dye solution, as is shown in Equation (4).

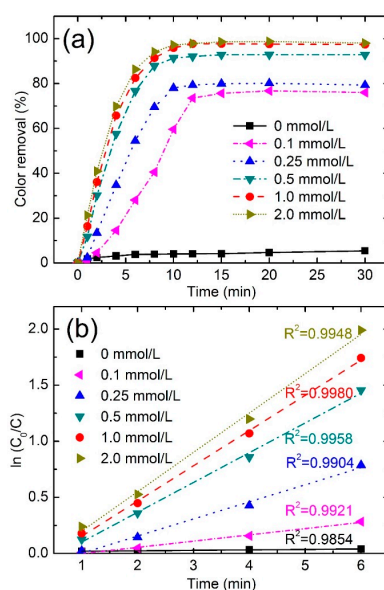


Figure 4. (a) Effect of PMS concentration on color removals in percentage vs. time; (b) variation of $\ln(C_0/C)$ vs. time at different PMS concentrations ($\text{Fe}_{78}\text{Si}_9\text{B}_{13}$ dosage: 0.5 g/L; dye concentration: 50 ppm; irradiation intensity: $7.7 \mu\text{W}/\text{cm}^2$).

Table 3. Color removal and reaction kinetics of various peroxymonosulfate (PMS) concentrations.

PMS Concentration (mmol/L)	Color Removal (%) at 4 min	Color Removal (%) at 8 min	Reaction Kinetics k (min^{-1})	R^2
0	3.2	3.9	0.004	0.9854
0.1	14.56	40.6	0.0557	0.9921
0.25	34.7	69.5	0.1526	0.9904
0.5	57.6	87.9	0.2654	0.9958
1.0	65.7	91.4	0.3140	0.9980
2.0	69.8	94.2	0.3509	0.9948

3.3.2. Effect of $\text{Fe}_{78}\text{Si}_9\text{B}_{13}$ Dosage

Figure 5 shows the effect of $\text{Fe}_{78}\text{Si}_9\text{B}_{13}$ dosage ranging from 0 to 2.0 g/L on the color removal of NGB dye under the following experimental conditions (PMS concentration: 1.0 mmol/L; irradiation intensity: $7.7 \mu\text{W}/\text{cm}^2$; and dye concentration: 50 ppm). It can be seen from Figure 5a, the NGB dye is almost completely degraded within 10 min at the ribbons dosage of 0.5 g/L, whereas 30 min is required to complete the degradation without $\text{Fe}_{78}\text{Si}_9\text{B}_{13}$ ribbons, indicating that the $\text{Fe}_{78}\text{Si}_9\text{B}_{13}$ ribbons can effectively activate PMS to produce reactive species. Further increases of ribbon dosage leads to slight effect of complete reaction time, where all of the reactions with addition of ribbons can reach more than 94% of color removal rate within 10 min. The first-order kinetic model is shown in Figure 5b and the corresponding data are summarized in Table 4. It can be seen from Table 4 that the reaction kinetics (k) value without $\text{Fe}_{78}\text{Si}_9\text{B}_{13}$ is 0.1489 min^{-1} while it is the double with adding ribbons dosage of 0.5 g/L, also confirming that PMS can be well activated by the $\text{Fe}_{78}\text{Si}_9\text{B}_{13}$ metallic glass. It is known that Fe^0 in the ribbons can directly react with PMS to produce $\text{SO}_4^{\bullet-}$ in the PMS solution (Equation (5)) [63]. Furthermore, with the enhancement of UV-vis irradiation, the corrosion of $\text{Fe}_{78}\text{Si}_9\text{B}_{13}$ ribbons are accelerated to provide more available Fe^{2+} (Equation (6)) [24]. The produced Fe^{2+} further reacts with PMS (Equation (7)). Sustainable generation of Fe^{2+} can be also achieved by Fe^{3+} reacting with Fe^0 (Equation (8)). As a result, the degradation rate of NGB is highly promoted.

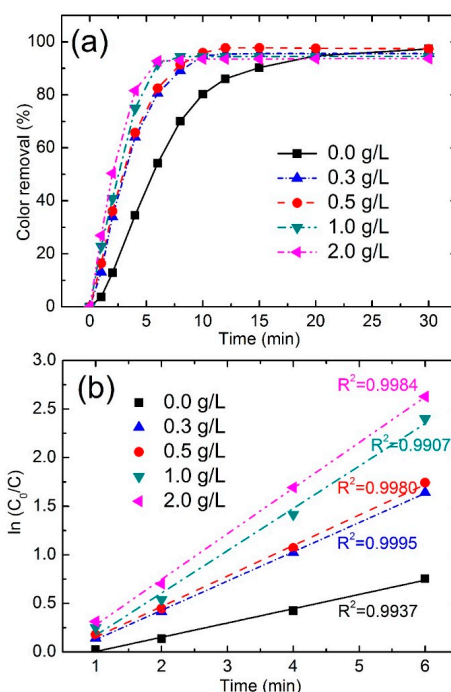


Figure 5. (a) Effect of $\text{Fe}_{78}\text{Si}_9\text{B}_{13}$ dosage on color removals in percentage vs. time; (b) variation of $\ln(C_0/C)$ vs. time at different $\text{Fe}_{78}\text{Si}_9\text{B}_{13}$ dosage (PMS concentration: 1.0 mmol/L; irradiation intensity: $7.7 \mu\text{W}/\text{cm}^2$; dye concentration: 50 ppm).

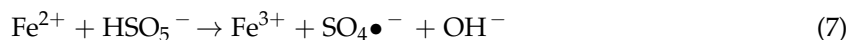
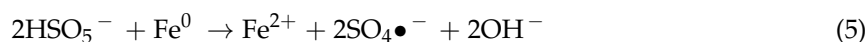


Table 4. Color removal and reaction kinetics of various $\text{Fe}_7\text{Si}_9\text{B}_{13}$ ribbons.

Dosage (g/L)	Color Removal (%) at 4 min	Color Removal (%) at 8 min	Reaction Kinetics k (min^{-1})	R^2
0	34.5	70.0	0.1489	0.9937
0.3	64.0	89.1	0.3011	0.9995
0.5	65.7	91.4	0.3140	0.9980
1.0	75.7	94.5	0.4357	0.9907
2.0	81.6	93.0	0.4691	0.9984

3.3.3. Effect of Irradiation Intensity

Figure 6a shows the effect of irradiation intensity varies from 0 to $14.8 \mu\text{W}/\text{cm}^2$ on color removal and the degradation rates of NGB dye using PMS activation by $\text{Fe}_7\text{Si}_9\text{B}_{13}$ ribbons. The first-order kinetic model is shown in Figure 6b and the corresponding data are summarized in Table 5. It is observed from Figure 6a that the dye removal rate with $\text{Fe}_7\text{Si}_9\text{B}_{13}$ ribbons alone present a relative fast efficiency, indicating that $\text{Fe}_7\text{Si}_9\text{B}_{13}$ metallic glass can activate PMS in a fast rate. On the other hand, the color removal rate reaches about 98% when the irradiation intensity increases from 0 to $7.7 \mu\text{W}/\text{cm}^2$, revealing that UV-vis irradiation can highly enhance the reactions. It is interesting to find that further increasing the irradiation intensity from 7.7 to $14.8 \mu\text{W}/\text{cm}^2$ results in a rapid increase of color removal rate at the first 4 min, especially at $14.8 \mu\text{W}/\text{cm}^2$, but all of them can almost complete the reaction in 8 min. As seen from Table 5, the color removal is more than 90% at 8 min with the irradiation intensity of $7.7 \mu\text{W}/\text{cm}^2$ or higher. Compared with $k = 0.5247 \text{ min}^{-1}$ using $14.8 \mu\text{W}/\text{cm}^2$ irradiation intensity, the reaction kinetics (k) is 0.0816 min^{-1} without the irradiation. It can be confirmed that the irradiation can effectively promote the color removal rate. The reasons for the enhancement by application of UV-vis irradiation are: (1) direct activation of PMS by UV-vis irradiation to produce $\text{SO}_4^{\bullet-}$ and $\bullet\text{OH}$ (Equation (9)); (2) sustainable generation of Fe^{2+} from Fe^{3+} under UV-vis irradiation and $\bullet\text{OH}$ at the same time (Equation (10)) [24]; (3) reaction between PMS and produced Fe^{2+} (Equation (7)).

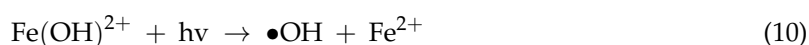


Table 5. Color removal and reaction kinetics of various irradiation intensities.

Irradiation Intensity ($\mu\text{W}/\text{cm}^2$)	Color Removal (%) at 4 min	Color Removal (%) at 8 min	Reaction Kinetics k (min^{-1})	R^2
0.0	28.7	50.1	0.0816	0.9989
7.7	65.7	91.4	0.2736	0.9980
11.1	74.7	93.9	0.314	0.9950
14.8	87.7	95.4	0.5247	0.9947

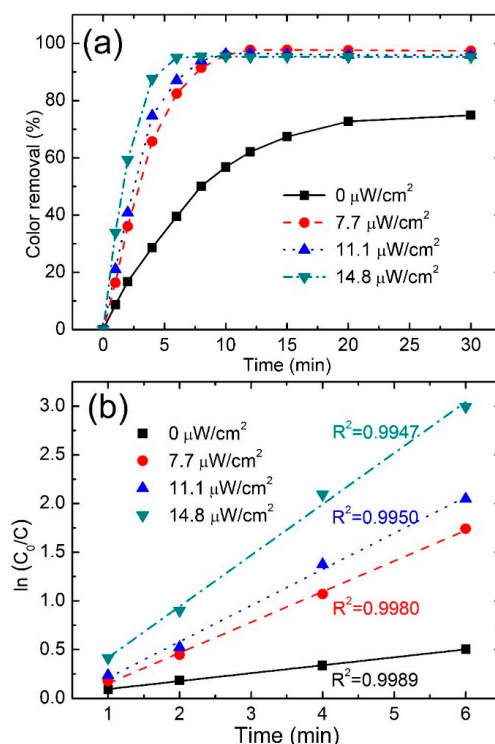


Figure 6. (a) Effect of irradiation intensity on color removals in percentage vs. time; (b) variation of $\ln(C_0/C)$ vs. time at different irradiation intensity (PMS concentration: 1.0 mmol/L; $\text{Fe}_7\text{Si}_9\text{B}_{13}$ dosage: 0.5 g/L; dye concentration: 50 ppm).

3.3.4. Effect of Dye Concentration

Figure 7a shows the color removal rate of the NGB dye with the concentration ranging from 10 to 100 ppm when other conditions are constant (PMS concentration: 1.0 mmol/L, $\text{Fe}_7\text{Si}_9\text{B}_{13}$ dosage: 0.5 g/L and irradiation intensity: 7.7 $\mu\text{W}/\text{cm}^2$). It is clear that the color removal rate decreases with the increase of NGB concentration. Compared with about 95% color removal rate at 6 min when degrading 10 ppm NGB, there is less than 70% color removal rate of 100 ppm NGB can be achieved at the same time. All the decolorization processes finish and reach the steady state within 12 min. Figure 7b shows the first-order kinetic model with the different dye concentrations and Table 6 shows the corresponding rate constants k . As seen from Table 6 the reaction kinetics k drops sharply from the highest value $k = 0.4566 \text{ min}^{-1}$ at 10 ppm dye concentration to $k = 0.2030 \text{ min}^{-1}$ at 100 ppm dye concentration. It means dye effluents can be decomposed better at lower concentration. The possible reason is higher dye concentration may block the light transmission to PMS, which results in lower activation of PMS to generate enough radicals [26]. Therefore, higher dye concentration has a lower color removal rate.

Table 6. Color removal and reaction kinetics of various dye concentrations.

NGB Concentration (ppm)	Color Removal (%) at 4 min	Color Removal (%) at 8 min	Reaction Kinetics k (min^{-1})	R^2
10	84.3	94.3	0.4566	0.9922
20	73.8	94.2	0.3841	0.9987
50	65.7	91.4	0.3140	0.9980
100	48.3	82.5	0.2032	0.9875

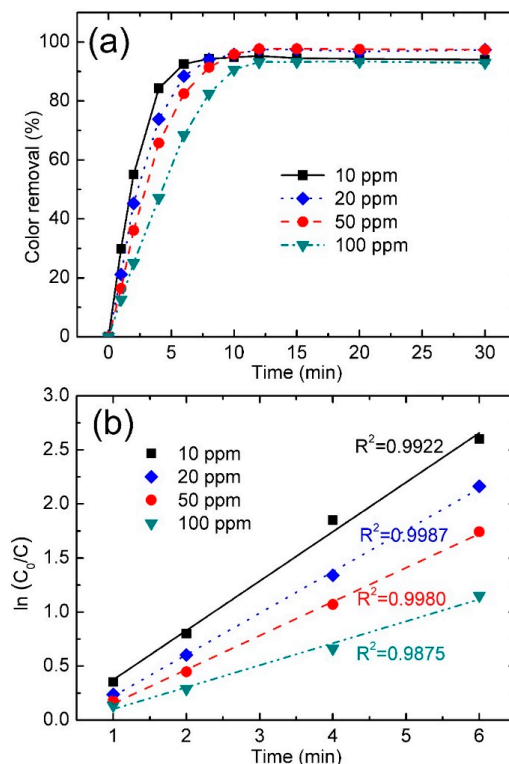


Figure 7. (a) Effect of dye concentration on color removals in percentage vs. time; (b) variation of $\ln(C_0/C)$ vs. time at different dye concentration (PMS concentration: 1.0 mmol/L; $\text{Fe}_{78}\text{Si}_9\text{B}_{13}$ dosage: 0.5 g/L; irradiation intensity: $7.7 \mu\text{W}/\text{cm}^2$).

3.3.5. Stability and Reusability

In order to study the surface stability and catalytic reusability of $\text{Fe}_{78}\text{Si}_9\text{B}_{13}$ ribbons, the same ribbons are reused 10 times. All the recycling experiments in this work are carried out on the same conditions (PMS concentration: 1.0 mmol/L; $\text{Fe}_{78}\text{Si}_9\text{B}_{13}$ dosage: 0.5 g/L; irradiation intensity: $7.7 \mu\text{W}/\text{cm}^2$; dye concentration: 50 ppm). Figure 8 shows the results of first, third, fifth, and tenth run of dye degradation with $\text{Fe}_{78}\text{Si}_9\text{B}_{13}$ ribbons. The corresponding data of the first-order kinetic model are summarized in Table 7. It can be seen that the NGB degradation rate is about 92% within 8 min for the first run and only very slightly decreases during third, fifth, and tenth run. Comparing the color removal rate and the reaction kinetics (k) of the first run with the tenth run, the color removal rate slight drops from 92.1% to 89.4% at 8 min and the reaction rate k decreases from 0.2997 to 0.2571 min^{-1} . It can be postulated that the product on the catalytic ribbons surface during the NGB degradation, as seen from Figure 2, which are crystallized $\alpha\text{-Fe}$, iron oxides and SiO_2 , slightly decrease the $\text{Fe}_{78}\text{Si}_9\text{B}_{13}$ catalytic efficiency [12]. Although, the weak bonding films form firstly during the dye degradation, with the help of vortex-stirrer, it is easy to fall off from the catalytic ribbon surface, which make it possible to continuously provide sufficient iron source for activating PMS. It is easy to find that there is no obvious difference between the results of fifth and tenth run. It reveals that $\text{Fe}_{78}\text{Si}_9\text{B}_{13}$ has excellent reusability in NGB degradation and can be run at least 10 times.

Table 7. Color removal and reaction kinetics of reused $\text{Fe}_{78}\text{Si}_9\text{B}_{13}$ ribbons.

Reused Times	Color Removal (%) at 4 min	Color Removal (%) at 8 min	Reaction Kinetics k (min^{-1})	R^2
first run	65.7	92.1	0.3170	0.9963
third run	62.7	90.1	0.2913	0.9933
fifth run	60.2	89.8	0.2811	0.9925
tenth run	58.6	89.4	0.2708	0.9946

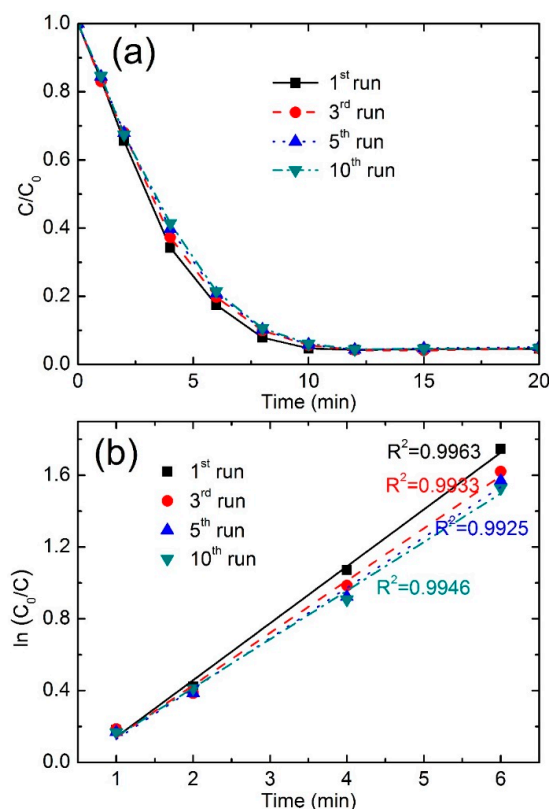


Figure 8. (a) NGB degradation with as-received and reused $\text{Fe}_{78}\text{Si}_9\text{B}_{13}$ ribbons; (b) variation of $\ln(C_0/C)$ vs. time of fresh and reused $\text{Fe}_{78}\text{Si}_9\text{B}_{13}$ ribbons (PMS concentration: 1.0 mmol/L; $\text{Fe}_{78}\text{Si}_9\text{B}_{13}$ dosage: 0.5 g/L; irradiation intensity: $7.7 \mu\text{W}/\text{cm}^2$; dye concentration: 50 ppm).

4. Conclusions

In this work, it is indicated that PMS could be effectively activated by $\text{Fe}_{78}\text{Si}_9\text{B}_{13}$ metallic glass for degrading NGB dye. The economic and efficient conditions can be concluded as 1.0 mmol/L PMS concentration, 0.5 g/L $\text{Fe}_{78}\text{Si}_9\text{B}_{13}$ ribbons dosage, and $7.7 \mu\text{W}/\text{cm}^2$ irradiation intensity. All the NGB degradation processes in this work fit well with the pseudo-first-order kinetic model. In addition, it is found that the NGB dye with a concentration of 50 ppm could be completely degraded within 10 min under the reasonable conditions of PMS concentration of 1.0 mmol/L, ribbons dosage of 0.5 g/L and irradiation intensity at $7.7 \mu\text{W}/\text{cm}^2$, which is faster than other reported materials [44,45].

According to the characterizations by XRD, UV-vis DRS, SEM, and EDS, the tenth run reused $\text{Fe}_{78}\text{Si}_9\text{B}_{13}$ ribbons only present a slight decay, indicating that the metallic glass can well retain the amorphous nature although it has been used for activating PMS 10 times. The precipitated substances on the tenth run ribbons surface are confirmed as α -Fe, iron oxides, and silicon oxide. The change of ribbon surface morphology indicates that oxide films with weak bonding on the surface were formed first, following with falling off, formation of compact films, and pitting corrosion when increasing reused time of ribbons.

The color removal rate of NGB dye increases with the increase of PMS concentration, $\text{Fe}_{78}\text{Si}_9\text{B}_{13}$ ribbons dosage and irradiation intensity. The recycling experiments show that $\text{Fe}_{78}\text{Si}_9\text{B}_{13}$ metallic glass can be reused for activating PMS more than 10 times with the excellent dye degradation rate, presenting a superior surface stability and reusability. The $\text{Fe}_{78}\text{Si}_9\text{B}_{13}$ metallic glass in this work receives a promising ability for activating PMS in NGB degradation and presents the potential wastewater treatment capacity for industrial scale in the future.

Acknowledgments: Financial supports from the ECU Innovator Awards (Project No. 23641), Australian Research Council Discovery Project (DP130103592) and National Science Foundation of China (Grant No. 61671206) are gratefully acknowledged. X.-F.L. appreciates the financial support from the Jiangsu Overseas Research & Training Program for University Prominent Young & Middle-aged Teachers and Presidents which is gratefully acknowledged.

Author Contributions: Xue-Fen Li, Shun-Xing Liang, Zhe Jia, and Lai-Chang Zhang conceived the experiments and wrote the manuscript. Xue-Fen Li, Shun-Xing Liang, and Zhe Jia conducted the experiments. Xue-Fen Li, Shun-Xing Liang, Xiao-Wang Xi, Zhe Jia, Shi-Kun Xie, He-Chun Lin, Jun-Ping Hu, and Lai-Chang Zhang analyzed the data. All authors reviewed the manuscript.

Conflicts of Interest: The authors declare no conflict of interest.

References

1. Zberg, B.; Uggowitzer, P.J.; Löffler, J.F. MgZnCa glasses without clinically observable hydrogen evolution for biodegradable implants. *Nat. Mater.* **2009**, *8*, 887–891. [[CrossRef](#)] [[PubMed](#)]
2. Henao, J.; Concustell, A.; Cano, I.G.; Dosta, S.; Cinca, N.; Guilemany, J.M.; Suhonen, T. Novel Al-based metallic glass coatings by cold gas spray. *Mater. Des.* **2016**, *94*, 253–261. [[CrossRef](#)]
3. Mariano, N.A.; Souza, C.A.C.; May, J.E.; Kuri, S.E. Influence of Nb content on the corrosion resistance and saturation magnetic density of FeCuNbSiB alloys. *Mater. Sci. Eng. A* **2003**, *354*, 1–5. [[CrossRef](#)]
4. Ghidelli, M.; Idrissi, H.; Gravier, S.; Blandin, J.J.; Raskin, J.P.; Schryvers, D.; Pardoën, T. Homogeneous flow and size dependent mechanical behavior in highly ductile Zr₆₅Ni₃₅ metallic glass films. *Acta Mater.* **2017**, *131*, 246–259. [[CrossRef](#)]
5. Ghidelli, M.; Gravier, S.; Blandin, J.J.; Raskin, J.P.; Lani, F.; Pardoën, T. Size-dependent failure mechanisms in ZrNi thin metallic glass films. *Scr. Mater.* **2014**, *89*, 9–12. [[CrossRef](#)]
6. Ghidelli, M.; Gravier, S.; Blandin, J.J.; Djemia, P.; Momprou, F.; Abadias, G.; Raskin, J.P.; Pardoën, T. Extrinsic mechanical size effects in thin ZrNi metallic glass films. *Acta Mater.* **2015**, *90*, 232–241. [[CrossRef](#)]
7. Ghidelli, M.; Gravier, S.; Blandin, J.J.; Pardoën, T.; Raskin, J.P.; Momprou, F. Compositional-induced structural change in Zr_xNi_{100-x} thin film metallic glasses. *J. Alloy. Compd.* **2014**, *615*, S348–S351. [[CrossRef](#)]
8. Ghidelli, M.; Volland, A.; Blandin, J.J.; Pardoën, T.; Raskin, J.P.; Momprou, F.; Djemia, P.; Gravier, S. Exploring the mechanical size effects in Zr₆₅Ni₃₅ thin film metallic glasses. *J. Alloy. Compd.* **2014**, *615*, S90–S92. [[CrossRef](#)]
9. Qin, X.D.; Zhu, Z.W.; Liu, G.; Fu, H.M.; Zhang, H.W.; Wang, A.M.; Li, H.; Zhang, H.F. Ultrafast degradation of azo dyes catalyzed by cobalt-based metallic glass. *Sci. Rep.* **2015**, *5*, 18226. [[CrossRef](#)] [[PubMed](#)]
10. Wang, J.Q.; Liu, Y.H.; Chen, M.W.; Louzguine-Luzgin, D.V.; Inoue, A.; Perepezko, J.H. Excellent capability in degrading azo dyes by MgZn-based metallic glass powders. *Sci. Rep.* **2012**, *2*, 418. [[CrossRef](#)] [[PubMed](#)]
11. Wang, P.; Wang, J.Q.; Li, H.; Yang, H.; Huo, J.; Wang, J.; Chang, C.; Wang, X.; Li, R.W.; Wang, G. Fast decolorization of azo dyes in both alkaline and acidic solutions by Al-based metallic glasses. *J. Alloy. Compd.* **2017**, *701*, 759–767. [[CrossRef](#)]
12. Jia, Z.; Zhang, W.C.; Wang, W.M.; Habibi, D.; Zhang, L.C. Amorphous Fe₇₈Si₉B₁₃ alloy: An efficient and reusable photo-enhanced Fenton-like catalyst in degradation of cibacron brilliant red 3B-A dye under UV-vis light. *Appl. Catal. B Environ.* **2016**, *192*, 46–56. [[CrossRef](#)]
13. Tang, Y.; Shao, Y.; Chen, N.; Liu, X.; Chen, S.Q.; Yao, K.F. Insight into the high reactivity of commercial Fe-Si-B amorphous zero-valent iron in degrading azo dye solutions. *RSC Adv.* **2015**, *5*, 34032–34039. [[CrossRef](#)]
14. Li, J.; Yang, L.; Ma, H.; Jiang, K.; Chang, C.; Wang, J.Q.; Song, Z.; Wang, X.; Li, R.W. Improved corrosion resistance of novel Fe-based amorphous alloys. *Mater. Des.* **2016**, *95*, 225–230. [[CrossRef](#)]
15. Deng, Z.; Zhang, X.H.; Chan, K.C.; Liu, L.; Li, T. Fe-based metallic glass catalyst with nanoporous surface for azo dye degradation. *Chemosphere* **2017**, *174*, 76–81. [[CrossRef](#)] [[PubMed](#)]
16. Wang, J.Q.; Liu, Y.H.; Chen, M.W.; Xie, G.Q.; Louzguine Luzgin, D.V.; Inoue, A.; Perepezko, J.H. Rapid degradation of azo dye by Fe-based metallic glass powder. *Adv. Funct. Mater.* **2012**, *22*, 2567–2570. [[CrossRef](#)]
17. Yang, J.F.; Bian, X.F.; Yuan, M.L.; Bai, Y.W.; Liu, Y.; Fan, J.P.; Lu, X.Q.; Song, K.K. Excellent degradation performance of azo dye by metallic glass/titanium dioxide composite powders. *J. Sol-Gel Sci. Technol.* **2013**, *67*, 362–367. [[CrossRef](#)]

18. Wang, P.P.; Wang, J.Q.; Huo, J.T.; Xu, W.; Wang, X.M.; Wang, G. Fast degradation of azo dye by nanocrystallized Fe-based alloys. *Sci. China Phys. Mech. Astron.* **2017**, *60*, 076112. [[CrossRef](#)]
19. Chen, S.Q.; Yang, G.N.; Luo, S.T.; Yin, S.J.; Jia, J.L.; Li, Z.; Gao, S.H.; Shao, Y.; Yao, K.F. Unexpected high performance of Fe-based nanocrystallized ribbons for azo dye decomposition. *J. Mater. Chem. A* **2017**, *5*, 14230–14240. [[CrossRef](#)]
20. Chen, S.Q.; Chen, N.; Cheng, M.T.; Luo, S.T.; Shao, Y.; Yao, K.F. Multi-phase nanocrystallization induced fast degradation of methyl orange by annealing Fe-based amorphous ribbons. *Intermetallics* **2017**, *90*, 30–35. [[CrossRef](#)]
21. Xie, S.; Huang, P.; Kruzic, J.J.; Zeng, X.; Qian, H. A highly efficient degradation mechanism of methyl orange using Fe-based metallic glass powders. *Sci. Rep.* **2016**, *6*, 21947. [[CrossRef](#)] [[PubMed](#)]
22. Liu, P.; Zhang, J.L.; Zha, M.Q.; Shek, C.H. Synthesis of an Fe rich amorphous structure with a catalytic effect to rapidly decolorize azo dye at room temperature. *ACS Appl. Mater. Interfaces* **2014**, *6*, 5500–5505. [[CrossRef](#)] [[PubMed](#)]
23. Jia, Z.; Duan, X.; Zhang, W.; Wang, W.; Sun, H.; Wang, S.; Zhang, L.C. Ultra-sustainable Fe₇₈Si₉B₁₃ metallic glass as a catalyst for activation of persulfate on methylene blue degradation under UV–vis light. *Sci. Rep.* **2016**, *6*, 38520. [[CrossRef](#)] [[PubMed](#)]
24. Jia, Z.; Kang, J.; Zhang, W.C.; Wang, W.M.; Yang, C.; Sun, H.; Habibi, D.; Zhang, L.C. Surface aging behaviour of Fe-based amorphous alloys as catalysts during heterogeneous photo Fenton-like process for water treatment. *Appl. Catal. B Environ.* **2017**, *204*, 537–547. [[CrossRef](#)]
25. Liu, F.J.; Yao, K.F.; Ding, H.Y. Fe-based glassy alloys with high iron content and high saturation magnetization. *Intermetallics* **2011**, *19*, 1674–1677. [[CrossRef](#)]
26. Liang, S.X.; Jia, Z.; Zhang, W.C.; Wang, W.M.; Zhang, L.C. Rapid malachite green degradation using Fe_{73.5}Si_{13.5}B₉Cu₁Nb₃ metallic glass for activation of persulfate under UV–vis light. *Mater. Des.* **2017**, *119*, 244–253. [[CrossRef](#)]
27. Mousavi Kouhi, S.M.; Lahouti, M.; Ganjeali, A.; Entezari, M.H. Comparative effects of ZnO nanoparticles, ZnO bulk particles, and Zn²⁺ on brassica napus after long-term exposure: Changes in growth, biochemical compounds, antioxidant enzyme activities, and Zn bioaccumulation. *Water Air Soil Pollut.* **2015**, *226*, 364. [[CrossRef](#)]
28. Jia, Z.; La, L.B.T.; Zhang, W.C.; Liang, S.X.; Jiang, B.; Xie, S.K.; Habibi, D.; Zhang, L.C. Strong enhancement on dye photocatalytic degradation by ball-milled TiO₂: A study of cationic and anionic dyes. *J. Mater. Sci. Technol.* **2017**. [[CrossRef](#)]
29. Prado, A.G.S.; Miranda, B.S.; Jacintho, G.V.M. Interaction of indigo carmine dye with silica modified with humic acids at solid/liquid interface. *Surf. Sci.* **2003**, *542*, 276–282. [[CrossRef](#)]
30. Karcher, S.; Kornmüller, A.; Jekel, M. Anion exchange resins for removal of reactive dyes from textile wastewaters. *Water Res.* **2002**, *36*, 4717–4724. [[CrossRef](#)]
31. Silva, G.C.; Ciminelli, V.S.T.; Ferreira, A.M.; Pissolati, N.C.; Paiva, P.R.P.; López, J.L. A facile synthesis of Mn₃O₄/Fe₃O₄ superparamagnetic nanocomposites by chemical precipitation: Characterization and application in dye degradation. *Mater. Res. Bull.* **2014**, *49*, 544–551. [[CrossRef](#)]
32. Jia, Z.; Miao, J.; Lu, H.B.; Habibi, D.; Zhang, W.C.; Zhang, L.C. Photocatalytic degradation and absorption kinetics of cibacron brilliant yellow 3G-P by nanosized ZnO catalyst under simulated solar light. *J. Taiwan Inst. Chem. Eng.* **2016**, *60*, 267–274. [[CrossRef](#)]
33. Miao, J.; Jia, Z.; Lu, H.B.; Habibi, D.; Zhang, L.C. Heterogeneous photocatalytic degradation of mordant black 11 with ZnO nanoparticles under UV–Vis light. *J. Taiwan Inst. Chem. Eng.* **2014**, *45*, 1636–1641. [[CrossRef](#)]
34. Jin, X.; Peldszus, S.; Huck, P.M. Reaction kinetics of selected micropollutants in ozonation and advanced oxidation processes. *Water Res.* **2012**, *46*, 6519–6530. [[CrossRef](#)] [[PubMed](#)]
35. Chu, W.; Ma, C.W. Quantitative prediction of direct and indirect dye ozonation kinetics. *Water Res.* **2000**, *34*, 3153–3160. [[CrossRef](#)]
36. Duan, X.; Sun, H.; Kang, J.; Wang, Y.; Indrawirawan, S.; Wang, S. Insights into heterogeneous catalysis of persulfate activation on dimensional-structured nanocarbons. *ACS Catal.* **2015**, *5*, 4629–4636. [[CrossRef](#)]
37. Bautista, P.; Mohedano, A.F.; Casas, J.A.; Zazo, J.A.; Rodriguez, J.J. An overview of the application of Fenton oxidation to industrial wastewaters treatment. *J. Chem. Technol. Biotechnol.* **2008**, *83*, 1323–1338. [[CrossRef](#)]
38. Dhakshinamoorthy, A.; Navalon, S.; Alvaro, M.; Garcia, H. Metal nanoparticles as heterogeneous Fenton catalysts. *ChemSusChem* **2012**, *5*, 46–64. [[CrossRef](#)] [[PubMed](#)]

39. Jia, Z.; Liang, S.X.; Zhang, W.C.; Wang, W.M.; Yang, C.; Zhang, L.C. Heterogeneous photo Fenton-like degradation of cibacron brilliant red 3B-A dye using amorphous $\text{Fe}_{78}\text{Si}_9\text{B}_{13}$ and $\text{Fe}_{73.5}\text{Si}_{13.5}\text{B}_9\text{Cu}_1\text{Nb}_3$ alloys: The influence of adsorption. *J. Taiwan Inst. Chem. Eng.* **2017**, *71*, 128–136. [[CrossRef](#)]
40. Sharma, J.; Mishra, I.M.; Dionysiou, D.D.; Kumar, V. Oxidative removal of Bisphenol A by UV-C/peroxymonosulfate (PMS): Kinetics, influence of co-existing chemicals and degradation pathway. *Chem. Eng. J.* **2015**, *276*, 193–204. [[CrossRef](#)]
41. Attallah, M.F.; Ahmed, I.M.; Hamed, M.M. Treatment of industrial wastewater containing congo red and naphthol green B using low-cost adsorbent. *Environ. Sci. Pollut. Res.* **2013**, *20*, 1106–1116. [[CrossRef](#)] [[PubMed](#)]
42. Riahi-Madvaar, R.; Taher, M.A.; Fazelirad, H. Synthesis and characterization of magnetic halloysite-iron oxide nanocomposite and its application for naphthol green B removal. *Appl. Clay Sci.* **2017**, *137*, 101–106. [[CrossRef](#)]
43. Saber, O.; El-Brolosy, T.A.; Al Jaafari, A.A. Improvement of photocatalytic degradation of naphthol green B under solar light using aluminum doping of Zinc oxide nanoparticles. *Water Air Soil Pollut.* **2012**, *223*, 4615–4626. [[CrossRef](#)]
44. Ameta, R.; Punjabi, P.B.; Ameta, S.C. Photodegradation of Naphthol green B in the presence of semiconducting antimony trisulphide. *J. Serbian Chem. Soc.* **2011**, *76*, 1049–1055. [[CrossRef](#)]
45. Kunkely, H.; Vogler, A. Photolysis of naphthol green B in aqueous solution. Photoreduction of Fe(III) induced by ligand-to-metal charge transfer excitation. *Z. Naturforsch. B* **2003**, *58*, 922–924.
46. Kumar, A.; Paliwal, M.; Ameta, R.; Ameta, S.C. A novel route for waste water treatment: Photo-assisted fenton degradation of naphthol green B. *Collect. Czechoslov. Chem. Commun.* **2008**, *73*, 679–689. [[CrossRef](#)]
47. Calin, M.; Zhang, L.C.; Eckert, J. Tailoring of microstructure and mechanical properties of a Ti-based bulk metallic glass-forming alloy. *Scr. Mater.* **2007**, *57*, 1101–1104. [[CrossRef](#)]
48. Zhang, L.C.; Shen, Z.Q.; Xu, J. Glass formation in a (Ti,Zr,Hf)-(Cu,Ni,Ag)-Al high-order alloy system by mechanical alloying. *J. Mater. Res.* **2003**, *18*, 2141–2149. [[CrossRef](#)]
49. Zhang, L.C.; Calin, M.; Branzel, M.; Schultz, L.; Eckert, J. Phase stability and consolidation of glassy/nanostructured $\text{Al}_{85}\text{Ni}_9\text{Nd}_4\text{Co}_2$ alloys. *J. Mater. Res.* **2007**, *22*, 1145–1155. [[CrossRef](#)]
50. Tang, Y.; Shao, Y.; Chen, N.; Yao, K.F. Rapid decomposition of direct blue 6 in neutral solution by Fe-B amorphous alloys. *RSC Adv.* **2015**, *5*, 6215–6221. [[CrossRef](#)]
51. Zhang, L.C.; Shen, Z.Q.; Xu, J. Mechanically milling-induced amorphization in Sn-containing Ti-based multicomponent alloy systems. *Mater. Sci. Eng. A* **2005**, *394*, 204–209. [[CrossRef](#)]
52. Zhang, L.C.; Kim, K.B.; Yu, P.; Zhang, W.Y.; Kunz, U.; Eckert, J. Amorphization in mechanically alloyed (Ti, Zr, Nb)-(Cu, Ni)-Al equiatomic alloys. *J. Alloy. Compd.* **2007**, *428*, 157–163. [[CrossRef](#)]
53. Zhang, L.C.; Xu, J. Glass-forming ability of melt-spun multicomponent (Ti, Zr, Hf)-(Cu, Ni, Co)-Al alloys with equiatomic substitution. *J. Non-Cryst. Solids* **2004**, *347*, 166–172. [[CrossRef](#)]
54. Zhang, L.C.; Xu, J.; Ma, E. Mechanically alloyed amorphous $\text{Ti}_{50}(\text{Cu}_{0.45}\text{Ni}_{0.55})_{44-x}\text{Al}_x\text{Si}_4\text{B}_2$ alloys with supercooled liquid region. *J. Mater. Res.* **2002**, *17*, 1743–1749. [[CrossRef](#)]
55. Ma, Y.; Rheingans, B.; Liu, F.; Mittemeijer, E.J. Isochronal crystallization kinetics of $\text{Fe}_{40}\text{Ni}_{40}\text{B}_{20}$ amorphous alloy. *J. Mater. Sci.* **2013**, *48*, 5596–5606. [[CrossRef](#)]
56. Huang, C.M.; Pan, G.T.; Li, Y.C.M.; Li, M.H.; Yang, T.C.K. Crystalline phases and photocatalytic activities of hydrothermal synthesis Ag_3VO_4 and $\text{Ag}_4\text{V}_2\text{O}_7$ under visible light irradiation. *Appl. Catal. A Gen.* **2009**, *358*, 164–172. [[CrossRef](#)]
57. Perezramirez, J. Active iron sites associated with the reaction mechanism of N_2O conversions over steam-activated FeMFI zeolites. *J. Catal.* **2004**, *227*, 512–522. [[CrossRef](#)]
58. Sun, K. Chemistry of N_2O decomposition on active sites with different nature: Effect of high-temperature treatment of Fe/ZSM-5. *J. Catal.* **2006**, *238*, 186–195. [[CrossRef](#)]
59. Koli, P. Study of enhanced photogalvanic effect of naphthol green B in natural sunlight. *J. Power Sources* **2015**, *285*, 310–317. [[CrossRef](#)]
60. Sun, H.; Zhou, G.; Liu, S.; Ang, H.M.; Tadé, M.O.; Wang, S. Nano- Fe^0 encapsulated in microcarbon spheres: Synthesis, characterization, and environmental applications. *ACS Appl. Mater. Interfaces* **2012**, *4*, 6235–6241. [[CrossRef](#)] [[PubMed](#)]

61. Cai, C.; Zhang, H.; Zhong, X.; Hou, L. Ultrasound enhanced heterogeneous activation of peroxymonosulfate by a bimetallic Fe-Co/SBA-15 catalyst for the degradation of orange II in water. *J. Hazard. Mater.* **2015**, *283*, 70–79. [[CrossRef](#)] [[PubMed](#)]
62. Lin, B.; Bian, X.; Wang, P.; Luo, G. Application of Fe-based metallic glasses in wastewater treatment. *Mater. Sci. Eng. B* **2012**, *177*, 92–95. [[CrossRef](#)]
63. Zhao, Y.F.; Si, J.J.; Song, J.G.; Yang, Q.; Hui, X.D. Synthesis of Mg-Zn-Ca metallic glasses by gas-atomization and their excellent capability in degrading azo dyes. *Mater. Sci. Eng. B* **2014**, *181*, 46–55. [[CrossRef](#)]



© 2017 by the authors. Licensee MDPI, Basel, Switzerland. This article is an open access article distributed under the terms and conditions of the Creative Commons Attribution (CC BY) license (<http://creativecommons.org/licenses/by/4.0/>).